Real-Time Visualization of Complexin During Single Exocytic Events

Seong J. An[1], **Chad P. Grabner**[1,2], and **David Zenisek**[1]

[1]Department of Cellular and Molecular Physiology, Yale University School of Medicine, New Haven, CT 06520, USA.

Abstract

Understanding the fundamental role of SNARE complexes in membrane fusion requires knowledge of the spatiotemporal dynamics of their assembly. To this end, we visualized complexin (cplx), a cytosolic protein that binds assembled SNARE complexes, during single exocytic events in live cells. We show that cplx appears briefly during full fusion. However, a truncated version of cplx containing only the SNARE-complex binding region persists at fusion sites for seconds and causes fusion to be transient. Resealing pores with the mutant cplx only partially release transmitter and lipid probes, indicating they are narrow and not purely lipidic in structure. Depletion of cplx similarly causes secretory cargo to be retained. Thus, complexin is recruited at a late step in exocytosis and modulates fusion pores composed of SNARE complexes.

Assembly of v- and t-SNAREs anchored respectively on vesicle and target membranes represents a critical step towards the formation of a fusion pore, the final step in membrane fusion, but how these two steps relate to each other remains unclear. In one view, they are energetically coupled and SNARE complex assembly drives membrane fusion1. Support for this comes from liposome fusion assays with purified SNAREs2 and amperometric detection of fusion pore properties in cells expressing modified SNAREs3,4. These studies invoke the existence of either a lipidic pore, formed through a hemifusion process catalyzed by SNARE complexes, or a protein-lined pore containing the transmembrane domains of v- and t-SNAREs5. In a fundamentally opposing view, the two steps are uncoupled6, and SNARE complexes enable downstream factors to ultimately form the fusion pore themselves7. How are SNARE complexes *intrinsically* fusogenic in some cases but not in others? Clearly, it would be helpful to study SNARE complex assembly at fusion sites in real time.

Here we investigated when and where SNARE complexes form during exocytosis in live cells by simultaneously observing cplx and secretory granules with total internal reflection fluorescence microscopy (TIRFM), a method that selectively illuminates fluorophores within 100 nm of the glass coverslip8. Cplx is a small, soluble protein that can bind either

tightly to the membrane-proximal half of the exocytic SNARE complex formed by the v-SNARE synaptobrevin (syb)/VAMP and the t-SNAREs syntaxin (syx) and SNAP25 (refs. 9–11), stabilizing the SNARE complex10, or weakly to the intermediate t-SNARE complex, preventing SNARE complex formation12–14. The dichotomy of its binding characteristics likely underlies the controversy surrounding its role in exocytosis15–18. By correlating its movements within cells to its impact on single fusion events, it was possible to distinguish between the modes of binding and learn more about the function of cplx as well as that of SNARE complexes.

RESULTS

Imaging complexin recruitment to release sites

Of the four mammalian isoforms of cplx, PC12 cells express only cplx 2 (Supplementary Fig. 1). We cotransfected PC12 cells with cplx 2 fused to green fluorescent protein (cplx-GFP) and neuropeptide Y fused to monomeric red fluorescent protein (NPY-mRFP), which localizes to secretory granules19. To favor detection of a small cplx signal, we selected cells weakly expressing cplx-GFP (see below). During stimulated exocytosis, docked granules brightened and then dimmed as they released NPY-mRFP (Fig. 1a). The initial brightening was largely due to the approach of NPY-mRFP toward the coverslip since neutralizing the acidic pH of granules increased mRFP fluorescence by only ~30% (Supplementary Fig. 2). When exocytic events were aligned to the first frame of fusion and averaged, a signal in the cplx-GFP channel became visible (Fig. 1a). The fluorescence peaked at the onset of fusion and had similar intensity before and after the peak. Though dim, the signal could not be accounted for by spectral bleed-through, which was negligible (Supplementary Fig. 3). Furthermore, no signal was observed when cells expressed a cplx-GFP mutant (R59,63E) unable to form critical salt bridges to syb (D57) in the SNARE complex (Fig. 1b; refs. 10, 11). Thus, the signal likely represented the recruitment of cplx-GFP by SNARE complexes during fusion.

Cplx contains a helical middle region that is the minimal SNARE-complex binding domain20. We made a deletion mutant corresponding to this domain, dubbed 'cplx short,' and mutants lacking either the N- or C-terminal region (Fig. 1f).   CT-GFP behaved similar to wildtype cplx-GFP (Fig. 1c), while   NT-GFP exhibited a slower time course of disappearance (Fig. 1d). By contrast, cplx short-GFP not only appeared at least 0.5 s prior to fusion but it also lingered much longer than wildtype cplx, ~2 s, before disappearing (Fig. 1e). These data show that cplx regions beyond the SNARE-complex binding domain affect the behavior of cplx. When wildtype cplx-GFP disappeared, it did so by laterally spreading (Supplementary Fig. 4), suggesting SNARE complexes diffused away from fusion sites. Spreading was less pronounced for   CT-GFP and not measurable for cplx short-GFP. The results shown in Figure 1a–e depict ensemble behavior of cplx-GFP constructs, averaged across all fusion events. These traces recapitulated individual events (Fig. 1g) and were similar to averages computed from averages of individual cells (Supplementary Fig. 5).

Little or no cplx colocalized with nonfusing granules on average, counter to the idea that complexin acts as a fusion clamp to prevent exocytosis15,16 (Supplementary Fig. 6). On the contrary, at the low expression levels required to detect SNARE complexes, all cplx

constructs increased the frequency of exocytic events compared to the R59,63E mutant, albeit to different degrees (Fig. 2). Interestingly, as its expression levels rose by over two orders of magnitude, wildtype cplx-GFP progressively decreased the frequency of exocytic events. This reversal appeared to require the C-terminal region of cplx since it was also manifested by NT-GFP but less so by the other deletion mutants. Thus, the effects of cplx on exocytosis are dependent on the concentration of cplx (see also Fig. 6b and Supplementary Fig. 12).

Persisting cplx causes transient fusion

Notably, granules released all or some NPY-mRFP, depending on which cplx construct appeared during fusion (Fig. 1a–e). This is better illustrated with NPY-mRFP traces normalized to their pre-fusion intensities (Fig. 3a, middle traces; Fig. 3b). To assay the rate granules released NPY-mRFP, we measured the loss of fluorescence within a 2.5-μm– diameter circle surrounding the granule after fusion (Fig. 3a, right traces; Fig. 3c). Figure 3e plots these release rates against the rates of cplx disappearance from fusion sites, which were fitted to single exponentials in Figure 3d. Evidently, the cplx mutants that resided longer at fusion sites were associated with slower release of NPY-mRFP from granules. Release rates were not correlated with granule intensity (Supplementary Fig. 7), and larger datasets of nonfusing granules showed little variation in average granule intensity (Supplementary Fig. 8).

Since longer cplx dwell time was correlated with slower and less complete release, we hypothesized that granules may reseal with cplx mutants that persist at fusion sites. To test this, we turned to tissue plasminogen activator (tPA), since this secretory protein is released more slowly than NPY, allowing granules to be monitored longer (Supplementary Fig. 9; ref. 19). Granules containing tPA fused to the highly pH-sensitive GFP-variant phluorin21 were invisible prior to exocytosis but brightened when their contents were exposed to neutral extracellular pH and then spread to different degrees (Fig. 4a). On average, the width of tPA-phluorin fluorescence, when fitted by a two-dimensional Gaussian function (see Methods), spread more quickly when cells expressed wildtype cplx than cplx short (0.76 ± 0.19 versus $0.33 \pm .03$ nm/s, $P = 0.00168$). Note that in these experiments cplx was fused to mRFP rather than GFP; it was not possible to reliably measure cplx-mRFP signals because of substantial bleedthrough (4.8%) of tPA-phluorin fluorescence.

When we alternately raised and lowered the external pH once a second, granules repeatedly brightened and dimmed as long as tPA-phluorin remained accessible to protons, i.e., unless resealing occurred (Fig. 4b; ref. 22). The fraction of granules that resealed within 100 s was 22% with no exogenous cplx, 40% with cplx short-mRFP and 17% with wildtype cplx-mRFP (Fig. 4c). The median time between fusion and resealing with no exogenous cplx was 4.25 s. Cplx short-mRFP reduced it to 2.5 s by tripling the frequency of fast resealing events (1.5 s) from 6% to 21%; in contrast, wildtype cplx-mRFP increased the median time to 41.5 s by appearing to prevent rapid resealing. Differences in resealing times among the three conditions were significant ($P < 0.001$, Kolmogorov-Smirnov tests; Fig. 4d). Thus, cplx short caused granules to only partially release NPY by promoting brief, transient fusion.

Lipid dyes poorly escape transient fusion pores

Since cplx binds SNARE complexes, its persistence during transient fusion suggests that fusion pores are relatively unexpanded. Accordingly, we explored the physical properties of resealing pores with lipid probes. The styryl dyes FM4-64 and FM1-84, a more lipophilic analog, were both less completely released with cplx short ($56 \pm 28\%$ and $64 \pm 16\%$ of the pre-fusion intensity after 4 s) than with wildtype cplx ($17 \pm 25\%$ and $22 \pm 19\%$) (Fig. 5a–d). However, the release rates for the dyes differed ~4-fold, reflecting either the known difference in their rates of departitioning[23] or a diffusional difference. To rule out the latter possibility, we used fluorescence recovery after photobleaching (FRAP) to examine their mobilities in PC12 plasma membranes (Supplementary Fig. 10). The measured diffusion coefficients for FM4-64 and FM1-84 were similar to each other (0.54 and 0.81 $\mu m^2/s$) and to those of other lipids in membranes[24], indicating that spreading alone cannot describe FM dye release.

Next, we investigated how dyes spread during release by quantifying their apparent diffusion coefficients. For this, we visually inspected every granule that fused to distinguish complete from incomplete release events. We found that 25% and 28% of granules released FM4-64 and FM1-84 incompletely when only endogenous cplx resided in cells (Supplementary Fig. 11g). These fractions increased to 38% and 48% with cplx short, and decreased to 14% and 15% with wildtype cplx, which is similar to the frequency of transient fusion witnessed under the different cplx conditions (see Fig. 4c). The kinetics of incomplete release events did not depend on the form of cplx expressed; in contrast, the rate of fluorescence rise of complete release events was greater with wildtype cplx than with cplx short (Supplementary Fig. 11a – f), suggesting that faster dilation of fusion pores caused resealing to be infrequent.

We fitted images of complete and incomplete release events from the cplx short dataset with radially symmetric Gaussian functions and plotted the width squared of these functions against time (Fig. 5e,g). The points were linearly related, suggestive of diffusive spreading[25], with slopes proportional to apparent diffusion coefficients of 0.45 and 0.15 $\mu m^2/s$ for complete and incomplete FM4-64 events, and 0.15 and 0.03 $\mu m^2/s$ for complete and incomplete FM1-84 events (Fig. 5f,h). Hence, during incomplete release, FM1-84 spread at a rate that was ~27 times smaller than its rate of diffusion; for FM4-64, the difference in rates was only 3.6-fold. Since both dyes have similar mobilities in membranes but different rates of departitioning[23], we conclude that the difference in apparent diffusion coefficients reflected low lipid permeability through a proteolipidic pore.

Cplx levels affect fusion pore dilation

Our results above predict that downregulation of cplx should slow down fusion pore dilation. To examine this possibility, we reduced cplx levels using RNA interference (RNAi). Cplx knockdown was ~90% effective (Fig. 6a), reducing evoked NPY-mRFP exocytosis in a bulk assay by 43% (Fig. 6b). This effect could be rescued with cplx-GFP, which by itself stimulated or inhibited exocytosis (by 34% or 14%) depending on the amount of cplx-GFP plasmid used to transfect cells. Even at a low, stimulatory amount of plasmid, the expression level of cplx-GFP was >20-fold greater than that of endogenous

cplx (Fig. 6c)—consistent with an inhibitory effect of cplx requiring very high cplx concentrations14 (see Fig. 2a). Stimulation of exocytosis by cplx-GFP was also observed when dopamine release was examined (Supplementary Fig. 12), further demonstrating that overexpression of cplx does not necessarily lead to inhibition of exocytosis18.

At the single cell level, using TIRFM, we observed $11 \pm 0.11\%$ of docked granules fuse during a 3.33 min recording period in control cells ($n = 77$ cells) but only $7.1 \pm 0.82\%$ do so in RNAi cells ($n = 119$ cells, $P = 0.00328$), in agreement with the bulk assay. Moreover, the latency of time to fusion increased with RNAi, such that the fraction of events occurring within the first 30 s of stimulation fell by more than a third, from 39% (187/480 events) to 24% (102/419 events) (Fig. 6d). Although not significantly different, the density of docked granules was slightly greater in RNAi cells than in control cells (1.2 ± 0.5 versus 1.0 ± 0.5 granules/μm^2) (Fig. 6e), indicating that cplx depletion did not grossly affect the pool size of releasable granules.

As expected, the extent of NPY-mRFP release (measured as % fluorescence remaining 4–5 s after fusion) was greater for granules in control cells ($69.9 \pm 0.1\%$) than in RNAi cells ($33.9 \pm 0.1\%$, $P = 0.00904$; Fig. 6f). Figure 6g displays the rates of release of NPY-mRFP from control and RNAi cells, along with those associated with wildtype cplx-GFP (solid line) and cplx short-GFP (dashed line), redisplayed from Figure 3c. The similarity of the slowed release rates with cplx short-GFP and with depleted levels of cplx suggests that cplx short-GFP exerted a dominant negative effect on fusion pore dilation. Note, however, that cplx short-GFP stimulated the frequency of exocytic events (see Fig. 2b), which indicates that its effect on dilation was independent of its ability to promote fusion.

Transmitter release is reduced during transient fusion

Amperometry was performed to examine how norepinephrine (NE) is released when fusion pores are pushed to dilate with wildtype cplx-GFP or reseal with cplx short-GFP. On average both the charge and amplitude of spikes from cells transfected with wildtype cplx-GFP were nearly twice as large as events measured from cells expressing cplx short-GFP (amplitude: 11.7 ± 1.9 versus 6.2 ± 0.7 pA; charge: 50.9 ± 10.8 versus 24.2 ± 2.1 fC) (Fig. 7a,b). Amplitude distributions revealed that small events produced by cplx short-GFP were tightly clustered at ~1.7 pA, sitting as a distinct peak beneath 3 pA (Fig. 7c). This peak was not discernible with wildtype cplx-GFP because amplitudes above 3 pA were more abundant, which is better appreciated in the cumulative plots (Fig. 7d). Several observations suggest that events below 3 pA represent resealing granules. First, their properties did not depend on which cplx was expressed (Fig. 7f,g), like the kinetics of incomplete FM dye release events (see Supplementary Fig. 11c,f). Second, events above 3 pA were larger with wildtype cplx-GFP than with cplx short-GFP (Fig. 7e,g), analogous to the greater rate of fluorescence rise when FM dye was released completely with wildtype cplx (see Supplementary Fig. 11b,e). Third, expression of cplx short promoted smaller events (44% <3 pA) as it did resealing frequency (40%), compared to expression of wildtype cplx (23% <3 pA; 17% resealing frequency).

Alternatively, smaller events produced by cplx short-GFP may be due to reduced loading of NE into granules. To test this, we utilized 5,7-dihydroxytryptamine (5,7-DHT), a fluorescent

analog of serotonin that, like NE, requires the action of vesicular monoamine transporters to accumulate in granules26 (Supplementary Fig. 13a,b). For this purpose, 5,7-DHT also served as a ratiometric pH indicator since it unexpectedly showed a robust (67-fold) change in its excitation ratio (365/381 nm) between pH 5.7 and 7.5 (Supplementary Fig. 13c,d). We found that cells expressing wildtype cplx, cplx short or no exogenous cplx not only took up similar amounts of 5,7-DHT, but also stored it at similar pH environments, consistent with that of granules (pH 5.5) (Supplementary Fig. 13f – h). No differences in granule density among the cplx conditions were observed that could influence 5,7-DHT signals (Supplementary Fig. 14). Taken together, these results argue that transient fusion, not reduced loading, caused events to be smaller in cells with cplx short. However, since granules resealed on the order of a couple seconds (see Fig. 4c), it is likely that factors other than pore open time determined the amount of transmitter release.

The above findings are in line with recent amperometric data showing that SNARE expression affects not only the prespike "foot" signal but also the spike itself4,27,28, which indicates that fusion pore dilation is a controlled process just like pore opening. Due to their small size, we were unable to ascertain whether events below 3 pA possessed a foot signal, but they were ostensibly different from stand-alone feet, which are rectangular in shape and caused by kiss-and-run events whose fusion pores fail to dilate29. Indeed, it is possible that events below 3 pA possessed a small but undetectable open state preceding the spike, since prolonged fusion pore openings (>1 s) can deplete free catecholamine in the granule30. For events over 3 pA, the foot duration was unchanged by the form of cplx expressed, but the charge per foot tended to be larger with wildtype cplx-GFP (5.85 ± 1.74 versus 3.62 ± 0.40 fC, $P = 0.14$) (Supplementary Fig. 15). Although the charge difference was not significant, overlaying ensemble averages to their rising phase revealed that wildtype cplx-GFP promoted a larger amplitude foot, suggesting that the pore opened to a wider initial state.

DISCUSSION

We show that cplx not only appears when fusion occurs, but also persists during transient fusion, for about the length of time it takes fusion pores to reseal. Since SNARE complex assembly is essential for exocytosis and complexin binds assembled SNARE complexes, we suggest that complexin is reporting productive SNARE complex assembly. Thus, our results support the idea that SNARE complexes make up the fusion apparatus1. Two initial pore structures are possible: The membrane anchors of SNAREs pack together to form a protein-lined pore akin to a gap junction channel that dilates by incorporating lipids3, or they stud the mouths of a partially lipid-lined pore27, guiding membrane mixing. The latter structure is expected to arise as SNARE complex assembly inexorably forces vesicle and target membranes into close proximity2,4. However, we observe a ~0.5 s interval between complexin recruitment and fusion onset with cplx short (see Fig. 1e), which suggests that proximity is insufficient for membranes to fuse. A delay in fusion may reflect a suboptimal number of SNARE complexes at fusion sites, but the finding that cplx short promotes exocytosis argues against this possibility. Rather, because fusion proceeds differently afterwards, it is likely that the delay reflects disordering of SNARE complexes. We propose that the fusogenicity of SNARE complexes critically depends on their spatial alignment. Since cplx deficiency affects the Ca^{2+}-sensitivity of transmitter release31, proper alignment

may be achieved through a collaborative effort between cplx and synaptotagmin, the likely Ca^{2+} sensor for exocytosis[32].

Studies of styryl dye release from neurons have provided evidence for both full fusion and kiss-and-run exocytosis of synaptic vesicles, based on the rate and extent of destaining (for review see ref. 33). In the case of neuroendocrine cells, complete release of FM4-64 has been reported even during transient exocytosis[34]. Our results demonstrate that the rate of FM dye departitioning from membranes limits dye release during fusion in a manner regulated by cplx, which suggests that multiple mechanisms of transient exocytosis may coexist. One possibility is that the dense core of the granule, if it remains intact, aids resealing through a process (e.g., dynamin-dependent endocytosis) that is distinct from the molecular reversal of fusion pore opening. The several-fold faster kinetics of FM4-64 release in the previous work is consistent with different sized transient fusion pores being observed. However, the relationship between pore size and styryl dye release kinetics is likely complicated by the interplay between dye association and dissociation in regions of high local lipid concentration, such as in small secretory organelles. Evidence of this interplay can be seen in the orders-of magnitude-difference in rates of departitioning observed in cellular preparations[23] and liposomes[35].

What is the role of cplx in exocytosis? Most cplx depletion studies point to a stimulatory role during a late, post-priming step in evoked release[18,31,36,37], although results are mixed regarding spontaneous release in neurons[38–40]. In contrast, overexpression studies and reconstituted fusion assays indicate that cplx acts as a fusion clamp[15,16,41–43]. These contradictory findings may reflect a complexity to cplx function that underlies the timing of neurotransmission[16,17]. However, it has recently been shown that cplx interacts with the intermediate t-SNARE complex[12,13] to block syb from entering into the SNARE complex[14], possibly by forming an alternative four-helix bundle[44]. In our study, cplx stimulates exocytosis at low expression levels, but inhibits it at much higher levels. The increase in expression needed for cplx to switch effects is comparable to the three-order-of-magnitude difference in its affinity for the SNARE complex and the t-SNARE complex ($Kd = 10–57$ nM versus ~50 μM; refs. 14, 45, 46). Thus, opposing phenotypes of cplx depletion and overexpression may reflect a biphasic function of cplx or an optimal concentration of cplx for exocytosis[47]. Unfortunately, since small cplx signals are lost in cells massively overexpressing cplx, it is not feasible to spatially investigate the inhibitory function.

The ability of cplx to dilate fusion pores is in contrast with reports that cplx reduces the size of amperometric spikes by promoting kiss-and-run[42] or that cplx promotes fusion but does not affect either the foot signal or the main spike[18]. Our proposed function of cplx (see Supplementary Fig. 16) is based not only on its influence on the release of several different types of cargo but also, importantly, on its movements during exocytosis, which are demonstrated here for the first time. Since proteins may influence fusion pore dynamics directly or indirectly (e.g., during vesicle biogenesis or docking), it is essential to correlate their effects with their activity inside cells. Our approach provides a way to do so and should help to clarify how the many proteins that interact with SNARE complexes control the opening and dilation of the fusion pore.

METHODS

Constructs

NPY-GFP and -mRFP plasmids were previously described19,48. To generate cplx-GFP, human cplx 2 (identical to rat cplx 2 in primary structure) was obtained from ATCC (clone # 6194391) and amplified by polymerase chain reaction (PCR) using the following primers: 5'-GGCGGCGGTACCCACCATGGC GGACTTCGTCATGAAGCA GGCC (sense), 5'-GGCGGCACCGGTGAACCACCAGAACCACCAGAACCACCAG AACCACCC TTCTTGAACATGTCCTGCAGCGG (antisense). The PCR product was subsequently ligated into the *Kpn*I/*Age*I site of pEGFP-N1 (Clontech). Short, NT and CT cplx mutants (see domain map in Fig. 1f) were amplified by using unique pairs of the above and following primers annealing to internal cplx sequences: 5'-GGCGGCG GTACCGGCCACCATGCTGCGGCAGCAGGAGGAGGA (sense; N-terminal deletion primer), 5'-GGCGGCACCGGTGAACCACCAGAACCACCAGAAC CACCAGAACC ACCGGGCCGGGTCAGGCTCCC (antisense; C-terminal deletion primer). The R59,63E mutant was made by site-directed mutagenesis (QuickChange, Stratagene). To generate cplx-mRFP constructs, mRFP was amplified with the primers 5'-GGCGGCAC CGGTCGCCACCATGGCCTCCTCCGAGGACGTC (sense) and 5'-GGCGGCGCGGC CGCTTAGGCGCCGGTGGAGTGG (antisense) and then ligated into *Age*I/*Not*I site of wildtype and short cplx-GFP vectors, replacing the ORF of GFP. In all cplx constructs, a 16 residue linker (GGSGGSGGSGGSPVAT) separated cplx from the first residue of GFP or mRFP. To generate tPA-mRFP, *Rattus rattus* tPA was obtained from ATCC (clone # 6920438) and amplified by using the following primers: 5'-GGCGGCAAGCT TAGCCCACCATGAAGGGAGAGCTGTTGTGCGTC (sense), 5'-GGCGGCGGTACC GTTTGCTTCATGTTGTCTTGGATCCAGTT (antisense). The PCR product was then ligated into the *Hin*dIII/*Kpn*I site of mRFP1. To fuse tPA to phluorin, we removed the coding sequence of mRFP from tPA-mRFP by digestion with AgeI and NotI and replaced it with the ORF of superecliptic phluorin amplified from transferrin receptor (Tfnr)-phluorin using the following primers: 5'-GGCGGCACCGGTGGGCGGCAGCGGCGG CAGCATGAGTAAAGGAGAAGAAC TTTTCACTGGAGTT (sense), 5'-GGCGGCG CGGCCGCTTATTTGTATAGTTCATCCATGCCATGTGTAAT (antisense). For knockdown, shRNA targeting coding sequence 136 to 156 in *Rattus norvegicus* cplx 2 was expressed by ligating the following oligonucelotides into pENTR/U6 (Clontech) after annealing them into the double-stranded form: 5'-CACCGAAGAGCGCAAGGCC AAACATCGAAATGTTTGGCCTTGCGCTCTTC (sense), 5'-AAAAGAAGAGCGCA AGGCCAAACATTTCGATGTTTGGCCTTGCGCTCTTC (antisense).

Immunoblotting

Immunoblotting was performed by standard methods with either Triton X-100 (1%, w/v) extracts of PC12 cells or rat brain synaptosomes. The following antibodies were used, all purchased from Synaptic Systems: syx 1 (mouse monoclonal, clone 78.2), SNAP25 (mouse monoclonal, clone 71.2); syb 2 (mouse monoclonal, clone 69.1); syt 1 (mouse monoclonal, clone 41.1); cplx 1, 2 (polyclonal rabbit); cplx 3 (mouse monoclonal, clone 294C2); cplx 4 (mouse monoclonal, clone 171H8). Blots were quantified with ImageJ software (National Institutes of Health).

Cells and solutions

PC12 GR5 stocks were maintained in T80 flasks (Nalgene/Nunc) at 37°C/10% CO_2 in DMEM high glucose (Invitrogen) supplemented with 5% new calf serum and 5% horse serum. Cells were replated to 30–50% confluence onto poly(L-lysine) (Sigma-Aldrich)-coated high refractive-index glass coverslips (n_{488} = 1.80; Plan Optik) and transiently transfected with ~2 μg plasmid DNA by *in situ* electroporation with five 40 ms 300V pulses in electroporation buffer (135 mM NaCl, 5 mM KCl, 25 mM Hepes, pH 7.4, and 25 mM glucose). To reduce cplx-GFP expression levels for imaging purposes, a 1:20 ratio of cplx to secretory cargo plasmid DNA was used in double transfections. For knockdown, cells were allowed to express shRNA for at least 60 h before imaging. During experiments, cells were bathed in extracellular buffer (130 mM NaCl, 2.8 mM KCl, 2 mM $CaCl_2$, 1 mM $MgCl_2$, 10 mM Hepes, 10 mM glucose, pH 7.4, 300 milliosmolal). To stimulate exocytosis, individual cells were locally perfused through a micropipette with a solution of elevated $[K^+]$ (105mM KCl, 50 mM NaCl, 2 mM $CaCl_2$, 0.7 mM $MgCl_2$, 1 mM NaH_2PO_4, 10 mM Hepes, pH 7.4, 330 milliosmolal). Experiments were carried out at room temperature (28°C).

TIRFM

Cells were viewed through an inverted microscope (Olympus IX-70) modified for objective-type evanescent-field illumination as previously described[8] using a 1.65 NA objective (Apo ×100 O HR, Olympus). Focusing was controlled using a PiFoc (PI-Polytec) piezo system and a low voltage differential transformer probe for feedback and stable focus control. An argon or a 488-nm solid state laser (Coherent Inc.) was used to excite green fluorophores, and a 561-nm solid state laser (Melles Griot) was used to excite red fluorophores simultaneously. Light entered and left the objective through a standard EGFP/dsRed filter set (Chroma #51019). A 565-nm dichroic mirror (Chroma Q565LP) in the image splitter (Dual-View, Optical Insights) then separated the transmitted fluorescence into green and red components, which respectively passed though a 50-nm band-pass filter centered at 525 nm and a 585-nm long-pass filter. The two components were projected as side-by-side images onto the back-illuminated chip of a charge-coupled device camera (Cascade 512B, Roper Scientific). For precise spatial alignment of green and red images, pictures of 100-nm beads fluorescing both green and red (Tetraspeck, Molecular Probes) were taken after each experiment and used as reference. Frames were acquired as streams at 33 Hz or in time-lapse recordings with 100-ms exposures given at 4 Hz using Metamorph software (Universal Imaging). Pixel size was 100 nm.

Image analysis

Granules undergoing exocytosis were identified by eye while movies were replayed. Onset of exocytosis was defined as the first frame showing a significant fluorescence increase of the granule. The time and location of each fusion event in a cell were noted and a 3.5×3.5-μm square area was centered on the brightest pixel of the granule and excised as a ministack for analysis. In two-color experiments, this square was transferred to the corresponding coordinates in the other-color image to produce a second ministack. Unless otherwise indicated, fluorescence of single granules was measured as the spatially averaged intensity difference between a 1.2-μm circle centered on the granule and a concentric annulus with a

1.2-μm inner and 2.5-μm outer diameter. In some experiments, the fluorescence of granules was fitted to the 2D Gaussian function $\exp(-r^2/\sigma^2)$, where r is the distance from the center of the granule and σ is the width parameter. For diffusive spread of material in a plane from an instantaneous point source, σ^2 is equal to $4Dt$, increasing linearly with time t and the apparent diffusion coefficient D.

FM-dye loading

Granules were labeled with FM4-64 as described[34]. At least 24 h after transfection, cells were incubated overnight with 6.4 μM FM4-64 (Molecular Probes). They were then thoroughly washed for 0.5–2 h in dye-free media. Granules were labeled with FM1-84 (purchased as synaptogreen C5 from Biotium) in the same manner.

Fast perfusion system

External pH was cycled as described[22]. Briefly, a theta glass capillary (World Precision Instruments) was pulled to ~50 μm tip size, and two polyimide tubes connected to pressurized reservoirs of pH 7.0 and 8.0 solutions (both containing 105 mM KCl to stimulate exocytosis) were inserted and sealed with glue. The tip of the perfusion pipette was positioned within 100 μm of the cell. Custom transistor-transistor logic (TTL) electronics were used to control solenoid pinch valves (Automate Scientific) and cycle between solutions. Before each experiment, cells expressing phluorin attached to the extracellular domain of transferrin receptor were imaged as solutions were slowly cycled at 0.1 Hz to determine the full-range of fluorescence intensity changes in response to pH. At faster cycling rates (1 Hz) used in resealing experiments, the solution exchange underneath the cell was slightly incomplete and the pH alternated, on average, between 7.1 and 7.8.

Confocal microscopy

Cells were imaged using a Yokagawa-type spinning disc confocal microscope system. The scan head (PerkinElmer) was mounted onto an inverted microscope (Olympus IX71) equipped with a 60×1.4 NA oil-immersion objective and an electron-multiplying charge-coupled device camera (Hamamatsu Photonics), which was controlled by Volocity software (Improvision). Excitation was achieved using 488- and 568-nm lines from an argon/krypton laser (Melles Griot). Exposure times were ~0.3 s. Pixel size was 143 nm. For determination of granule density in cells, a semi-automated method employing ImageJ software (National Institutes of Health) was used. Briefly, five 0.5-μm thick Z-sections closest to the coverslip for each cell were summed into a single 8-bit image, processed with a Laplacian of Gaussian filter, inverted and thresholded. Granules were then counted automatically using a particle analysis program.

FRAP

FM dye (6.4 μM) was diluted onto cells plated on poly(L-lysine)-coated glass bottom culture dishes (MatTek). Cells were immediately viewed using a confocal microscope (Zeiss LSM510) equipped with a $63 \times$ oil-immersion objective (1.4 NA Plan Apochromat). Images were acquired every 393 ms. The pinhole was selected to collect a 0.9 μm optical slice containing the portion of the cell membrane adhered to glass. A circular area (~4.5-μm

diameter) was bleached with 25 scanning iterations at full power output. Fluorescence intensity was calculated using the histogram function available in the LSM510 software. Diffusion coefficients49 were calculated via the equation $D = (\omega^2/4\tau)\gamma$ where ω is the width of the bleached region at e^{-2} of the peak height, τ is the observed half-time of recovery and γ is a correction factor for the amount of bleaching, which was set as 1.

Bulk NPY-mRFP and dopamine release assays

Cells transfected with NPY-mRFP and other plasmids were incubated in extracellular buffer with or without 90 mM KCl. After 45 min at 28°C, the buffer was collected, and the cells were washed three times, solubilized with 1% Triton X-100 for 10 min and then pelleted in an eppendorf tube at 16,000g for 5 min. NPY-mRFP fluorescence in the buffer and the soluble fraction of the detergent extract was measured using a FluoroMax-3 Spectrophotometer (HORIBA Jobin Yvon) running DataMax software with the following settings: excitation wavelength, 580 nm; emission wavelength, 620 nm; slit width for both excitation and emission, 5 nm; integration time, 10 s. For dopamine release experiments, cells in 6-well dishes were incubated with dopamine (1 mM) in the presence of ascorbic acid (1 mM) for 60 min at 37°C. The cells were quickly washed three times in cold extracellular solution and then further incubated with low or high [K$^+$] for 5 min. After stimulation, total cellular dopamine was extracted by solubilizing cells in 1% TX-100. Dopamine was detected using an enzyme-linked immunosorbent assay (GenWay Biotech Inc., San Diego, CA) in the linear range of detection.

5,7-DHT uptake

For *in vitro* fluorescence measurements, 5,7-DHT (Sigma-Aldrich) was dissolved in solutions of monosodium phosphate and disodium phosphate adjusted to varying pH values. For uptake experiments, cells grown on 6-well dishes or 75-cm^2 flasks were incubated with varying concentrations of 5,7-DHT in extracellular buffer for 1–2 h at 37°C. NaCl concentration was reduced when 5,7-DHT was used at 20 mM, to keep the osmolarity constant. Where indicated, reserpine or its dimethylsulfoxide vehicle (control) was added with 5,7-DHT. For uptake measurements *in situ*, cells were lifted from dishes by gentle scraping, or from flasks by chelating Ca^{2+} and Mg^{2+} with versene (Invitrogen), and kept in suspension by stirring. Emission and excitation spectra were scanned in 1-nm increments, with an integration time of 0.5 s and both emission and excitation slit widths at 5 nm.

Amperometry

Carbon fiber electrodes were fabricated as described50. Amperometric recordings were made with an EPC-10 amplifier (HEKA Electronics). The carbon fiber electrode was held at +750 mV relative to the silver-chloride ground electrode in the bath. Currents were collected at 10 kHz, and filtered at 2.9 kHz with a low pass Bessel filter. Events were analyzed with MiniAnalysis software (Synaptosoft). Traces were filtered offline to an effective corner frequency of 1 kHz using a Gaussian filter, and only recordings with root-mean-square noise under 1 pA were analyzed. The event detection threshold was set to 4 × rms noise. Events were aligned to their rising phase at 50% amplitude, and overlapping events were excluded

from the analysis. Individual spike parameters were averaged within cell, and the level of significance between groups was examined with the Mann-Whitney test.

Statistics

Data are expressed as averages ± s.e.m. Unless otherwise noted, unpaired two-tailed Student's *t*-tests were used to test for statistical significance.

Supplementary Material

Refer to Web version on PubMed Central for supplementary material.

ACKNOWLEDGEMENTS

REFERENCES

1. Jahn R, Scheller RH. SNAREs—engines for membrane fusion. Nature Rev. Mol. Cell Biol. 2006; 7:631–643. [PubMed: 16912714]

2. Weber T, et al. SNAREpins: minimal machinery for membrane fusion. Cell. 1998; 92:759–772. [PubMed: 9529252]

3. Han X, Wang CT, Bai J, Chapman ER, Jackson MB. Transmembrane segments of syntaxin line the fusion pore of Ca^{2+}-triggered exocytosis. Science. 2004; 304:289–292. [PubMed: 15016962]

4. Kesavan J, Borisovska M, Bruns D. v-SNARE actions during Ca^{2+}-triggered exocytosis. Cell. 2007; 131:351–363. [PubMed: 17956735]

5. Jackson MB, Chapman ER. Fusion pores and fusion machines in Ca^{2+}-triggered exocytosis. Annu. Rev. Biophys. Biomol. Struct. 2006; 35:135–160. [PubMed: 16689631]

6. Ungermann C, Sato K, Wickner W. Defining the functions of trans-SNARE pairs. Nature. 1998; 396:543–548. [PubMed: 9859990]

7. Peters C, et al. Trans-complex formation by proteolipid channels in the terminal phase of membrane fusion. Nature. 2001; 409:581–588. [PubMed: 11214310]

8. Merrifield CJ, Feldman ME, Wan L, Almers W. Imaging actin and dynamin recruitment during invagination of single clathrin-coated pits. Nature Cell Biol. 2002; 4:691–698. [PubMed: 12198492]

9. McMahon HT, Missler M, Li C, Südhof TC. Complexins: cytosolic proteins that regulate SNAP receptor function. Cell. 1995; 83:111–119. [PubMed: 7553862]

10. Chen X, et al. Three-dimensional structure of the complexin/SNARE complex. Neuron. 2002; 33:397–409. [PubMed: 11832227]

11. Bracher A, Kadlec J, Betz H, Weissenhorn W. X-ray structure of a neuronal complexin-SNARE complex from squid. J. Biol. Chem. 2002; 277:26517–26523. [PubMed: 12004067]

12. Weninger K, Bowen ME, Choi UB, Chu S, Brunger AT. Accessory proteins stabilize the acceptor complex for synaptobrevin, the 1:1 syntaxin/SNAP-25 complex. Structure. 2008; 16:308–320. [PubMed: 18275821]

13. Guan R, Dai H, Rizo J. Binding of the Munc13-1 MUN domain to membrane-anchored SNARE complexes. Biochemistry. 2008; 47:1474–1481. [PubMed: 18201107]

14. Yoon TY, et al. Complexin and Ca^{2+} stimulate SNARE-mediated membrane fusion. Nature Struct. Mol. Biol. 2008; 15:707–713. [PubMed: 18552825]

15. Giraudo CG, Eng WS, Melia TJ, Rothman JE. A clamping mechanism involved in SNARE-dependent exocytosis. Science. 2006; 313:676–680. [PubMed: 16794037]

16. Tang J, et al. A complexin/synaptotagmin 1 switch controls fast synaptic vesicle exocytosis. Cell. 2006; 126:1175–1187. [PubMed: 16990140]

17. Xue M, et al. Distinct domains of complexin I differentially regulate neurotransmitter release. Nature Struct. Mol. Biol. 2007; 14:949–958. [PubMed: 17828276]

18. Cai H, et al. Complexin II plays a positive role in Ca^{2+}-triggered exocytosis by facilitating vesicle priming. Proc. Natl Acad. Sci. USA. 2008; 105:19538–19543. [PubMed: 19033464]

19. Taraska JW, Perrais D, Ohara-Imaizumi M, Nagamatsu S, Almers W. Secretory granules are recaptured largely intact after stimulated exocytosis in cultured endocrine cells. Proc. Natl Acad. Sci. USA. 2003; 100:2070–2075. [PubMed: 12538853]

20. Pabst S, et al. Selective interaction of complexin with the neuronal SNARE complex. Determination of the binding regions. J. Biol. Chem. 2000; 275:19808–19818. [PubMed: 10777504]

21. Miesenböck G, De Angelis DA, Rothman JE. Visualizing secretion and synaptic transmission with pH-sensitive green fluorescent proteins. Nature. 1998; 394:192–195. [PubMed: 9671304]

22. Perrais D, Kleppe IC, Taraska JW, Almers W. Recapture after exocytosis causes differential retention of protein in granules of bovine chromaffin cells. J. Physiol. 2004; 560:413–428. [PubMed: 15297569]

23. Ryan TA, Smith SJ, Reuter H. The timing of synaptic vesicle endocytosis. Proc. Natl Acad. Sci. USA. 1996; 93:5567–5571. [PubMed: 8643616]

24. Pucadyil TJ, Chattopadhyay A. Effect of cholesterol on lateral diffusion of fluorescent lipid probes in native hippocampal membranes. Chem. Phys. Lipids. 2006; 143:11–21. [PubMed: 16797513]

25. Schmoranzer J, Goulian M, Axelrod D, Simon SM. Imaging constitutive exocytosis with total internal reflection fluorescence microscopy. J. Cell Biol. 2000; 149:23–32. [PubMed: 10747084]

26. Corcoran JJ, Wilson SP, Kirshner N. Flux of catecholamines through chromaffin vesicles in cultured bovine adrenal medullary cells. J. Biol. Chem. 1984; 259:6208–6214. [PubMed: 6725249]

27. Fang Q, et al. The role of the C terminus of the SNARE protein SNAP-25 in fusion pore opening and a model for fusion pore mechanics. Proc. Natl Acad. Sci. USA. 2008; 105:15388–15392. [PubMed: 18829435]

28. Bretou M, Anne C, Darchen F. A fast mode of membrane fusion dependent on tight SNARE zippering. J. Neurosci. 2008; 28:8470–8476. [PubMed: 18716205]

29. Wang CT, et al. Different domains of synaptotagmin control the choice between kiss-and-run and full fusion. Nature. 2003; 424:943–947. [PubMed: 12931189]

30. Gong LW, de Toledo GA, Lindau M. Exocytotic catecholamine release is not associated with cation flux through channels in the vesicle membrane but Na+ influx through the fusion pore. Nature Cell Biol. 2007; 9:915–922. [PubMed: 17643118]

31. Reim K, et al. Complexins regulate a late step in Ca^{2+}-dependent neurotransmitter release. Cell. 2001; 104:71–81. [PubMed: 11163241]

32. Chapman ER. Synaptotagmin: a Ca^{2+} sensor that triggers exocytosis? Nature Rev Mol.Cell Biol. 2002; 3:498–508. [PubMed: 12094216]

33. An S, Zenisek D. Regulation of exocytosis in neurons and neuroendocrine cells. Curr. Opin. Neurobiol. 2004; 14:522–530. [PubMed: 15464884]

34. Taraska JW, Almers W. Bilayers merge even when exocytosis is transient. Proc. Natl Acad. Sci. USA. 2004; 101:8780–8785. [PubMed: 15173592]

35. Wu Y, Yeh FL, Mao F, Chapman ER. Biophysical characterization of styryl dye-membrane interactions. Biophys. J. 2009; 97:101–109. [PubMed: 19580748]

36. Abderrahmani A, et al. Complexin I regulates glucose-induced secretion in pancreatic beta-cells. J. Cell. Sci. 2004; 117:2239–2247. [PubMed: 15126625]

37. Tadokoro S, Nakanishi M, Hirashima N. Complexin II facilitates exocytotic release in mast cells by enhancing Ca^{2+} sensitivity of the fusion process. J. Cell Sci. 2005; 118:2239–2246. [PubMed: 15870114]

38. Huntwork S, Littleton JT. A complexin fusion clamp regulates spontaneous neurotransmitter release and synaptic growth. Nature Neurosci. 2007; 10:1235–1237. [PubMed: 17873870]

39. Xue M, et al. Complexins facilitate neurotransmitter release at excitatory and inhibitory synapses in mammalian central nervous system. Proc. Natl Acad. Sci USA. 2008; 105:7875–7880. [PubMed: 18505837]

40. Maximov A, Tang J, Yang X, Pang ZP, Südhof TC. Complexin controls the force transfer from SNARE complexes to membranes in fusion. Science. 2009; 323:516–521. [PubMed: 19164751]

41. Itakura M, Misawa H, Sekiguchi M, Takahashi S, Takahashi M. Transfection analysis of functional roles of complexin I and II in the exocytosis of two different types of secretory vesicles. Biochem. Biophys. Res. Commun. 1999; 265:691–696. [PubMed: 10600482]

42. Archer DA, Graham ME, Burgoyne RD. Complexin regulates the closure of the fusion pore during regulated vesicle exocytosis. J. Biol. Chem. 2002; 277:18249–18252. [PubMed: 11929859]

43. Schaub JR, Lu X, Doneske B, Shin YK, McNew JA. Hemifusion arrest by complexin is relieved by Ca^{2+}-synaptotagmin I. Nature Struct. Mol. Biol. 2006; 13:748–750. [PubMed: 16845390]

44. Giraudo CG, et al. Alternative zippering as an on-off switch for SNARE-mediated fusion. Science. 2009; 323:512–516. [PubMed: 19164750]

45. Pabst S, et al. Rapid and selective binding to the synaptic SNARE complex suggests a modulatory role of complexins in neuroexocytosis. J. Biol. Chem. 2002; 277:7838–7848. [PubMed: 11751907]

46. Li Y, Augustine GJ, Weninger K. Kinetics of complexin binding to the SNARE complex: correcting single molecule FRET measurements for hidden events. Biophys. J. 2007; 93:2178–2187. [PubMed: 17513363]

47. Edwardson JM, et al. Expression of mutant huntingtin blocks exocytosis in PC12 cells by depletion of complexin II. J. Biol. Chem. 2003; 278:30849–30853. [PubMed: 12807877]

48. An SJ, Almers W. Tracking SNARE complex formation in live endocrine cells. Science. 2004; 306:1042–1046. [PubMed: 15528447]

49. Axelrod D, Koppel DE, Schlessinger J, Elson E, Webb WW. Mobility measurement by analysis of fluorescence photobleaching recovery kinetics. Biophys. J. 1976; 16:1055–1069. [PubMed: 786399]

50. Grabner CP, Price SD, Lysakowski A, Fox AP. Mouse chromaffin cells have two populations of dense core vesicles. J. Neurophysiol. 2005; 94:2093–2104. [PubMed: 15944233]
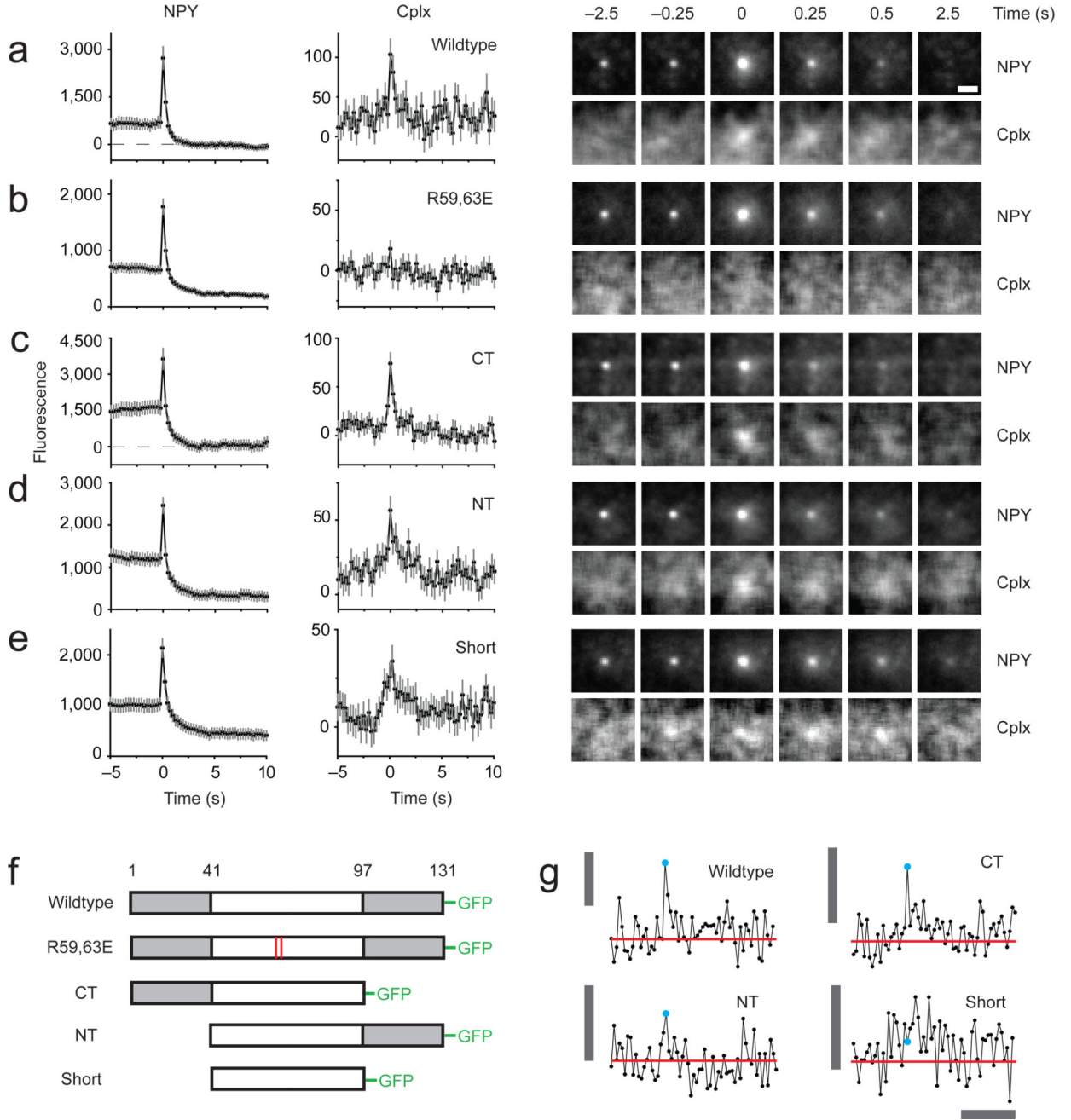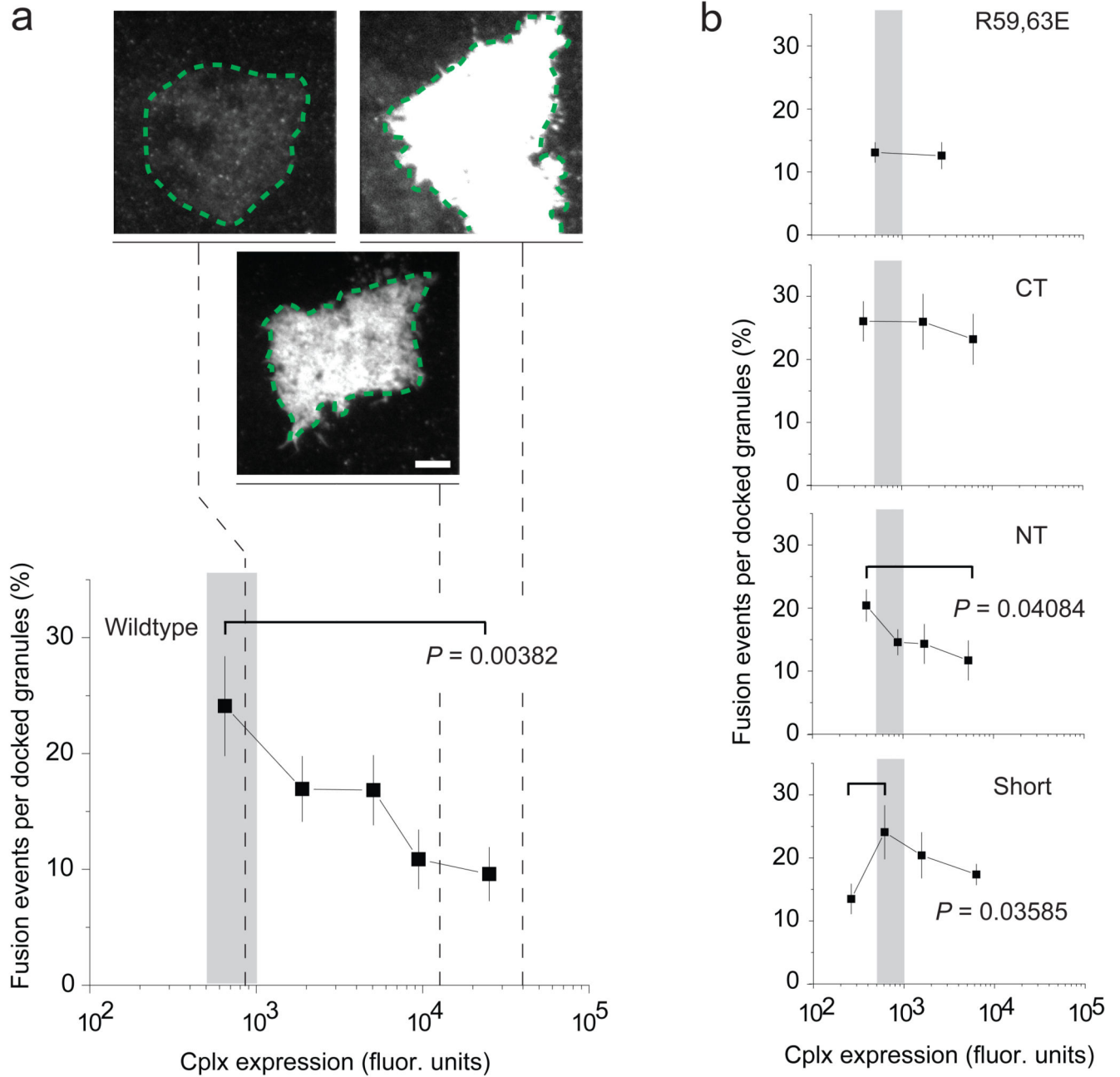
Figure 1.

Imaging secretory granules labeled with NPY-mRFP undergoing exocytosis in PC12 cells coexpressing different versions of cplx-GFP. (**a**–**e**) Images (right) are averages of events time-aligned to the moment of fusion: wildtype ($n = 94$ events, 11 cells), R59,63E ($n = 139$ events, 16 cells), CT ($n = 85$ events, 10 cells), NT ($n = 144$ events, 18 cells), 'short' ($n = 123$ events, 12 cells). The fluorescence intensity (left) was calculated by taking the average intensity within a 1.2-μm circle centered on a granule, or the corresponding coordinates in the cplx channel, and subtracting the average intensity within a concentric 1.3-μm wide

annulus, which served as the local background fluorescence; intensities were plotted against time and then averaged. Exocytosis was stimulated by perfusion with a solution of elevated [K$^+$]. 3–6 transfections were performed per condition. Scale bar, 1 μm. Error bars are ± s.e.m. (**f**) Schematic diagram of cplx-GFP fusion proteins. (**g**) Examples of cplx-GFP signals associated with single fusion events. Cyan circle indicates when fusion occurred. Red line is the average intensity in the trace 3–5 s before fusion. Vertical bar, 200 fluorescence units; horizontal bar, 5 s.

Figure 2.
Effect of cplx overexpression on NPY-mRFP exocytosis. (**a**) Plot of fusion events (% of docked granules) versus cplx expression level. The recording period was 3.33 min. The spatially averaged cplx-GFP fluorescence of the 'footprint' of the cell, where the cell adhered closely to the coverslip (green dashed lines), served as a measure of expression. The cplx expression levels of cells required for detecting SNARE complexes (see Fig. 1) fell within the range indicated by the shaded area (~500–1,000 fluorescence units). Representative footprints are shown at the same contrast setting to illustrate the differences in the brightness of transfected cells. Scale bar, 10 μm. (**b**) As in **a**, but for other cplx

constructs. All points are the average of a 20-cell bin, except for the rightmost point in each plot, which represented the following number of cells: 17 (wildtype), 15 (R59,63E), 15 (ΔCT), 24 (ΔNT) and 18 (short). 3–8 transfections were performed per condition. Error bars are ± s.e.m. *P* values determined using a Student's *t*-test.
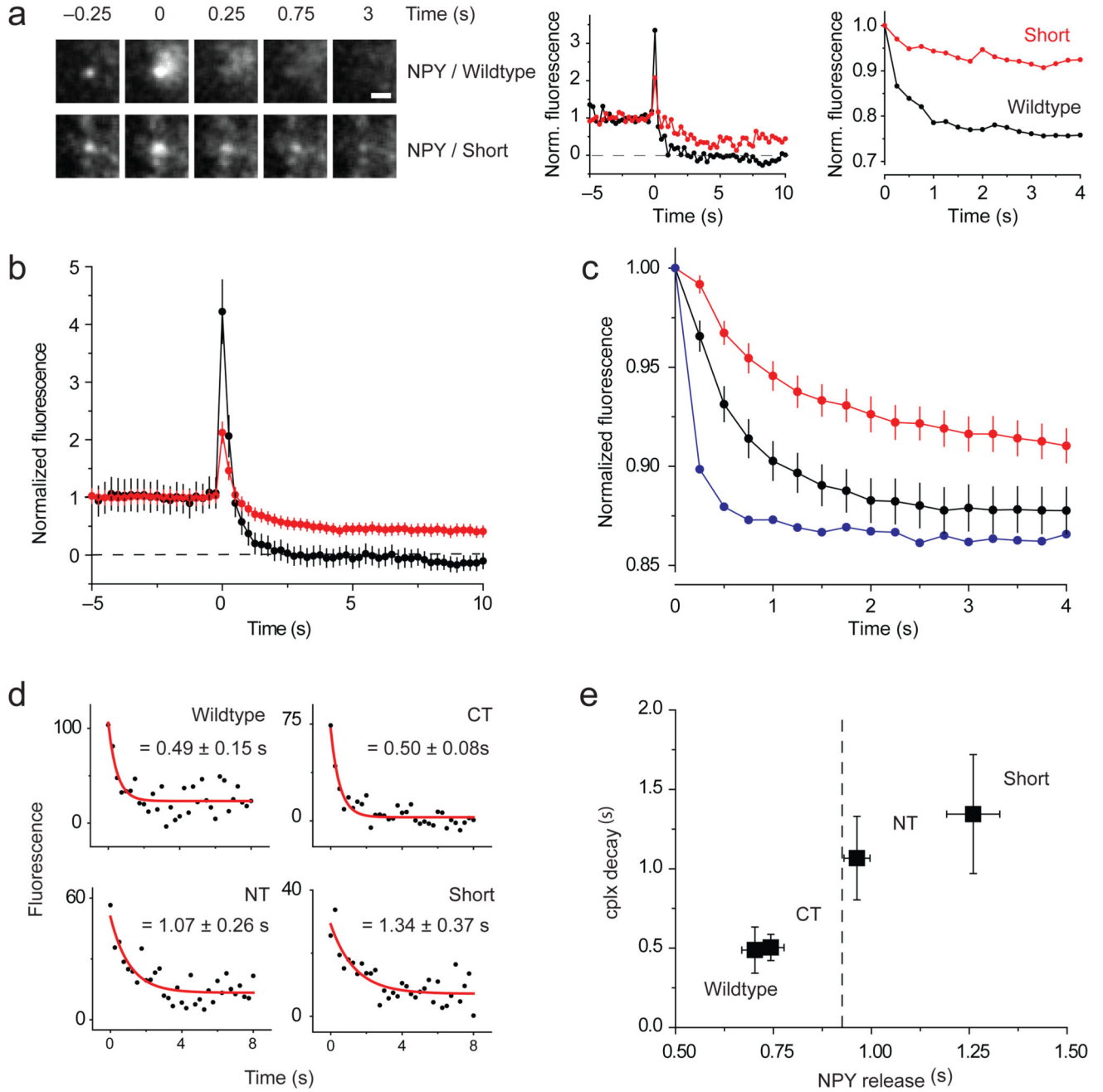
Figure 3.
Slow and incomplete release of NPY-mRFP when cplx persists during fusion. (**a**) Images (left) of granules releasing NPY-mRFP completely with wildtype cplx-GFP or incompletely with cplx short-GFP. Scale bar, 1 μm. (Middle) Background-subtracted fluorescence of same granules, normalized to the intensity during the last 2 s before fusion. (Right) Average fluorescence within larger, 2.5-μm–diameter circles centered over same granules, normalized to the intensity when fusion occurred. This 'outer-circle' fluorescence analysis is a better measure of the rate of NPY-mRFP release, since it minimizes diffusional loss

outside of the region of interest. (**b**) Averages of background-subtracted NPY-mRFP fluorescence traces in Figure 1a,e normalized to pre-fusion intensity. Black trace, wildtype cplx-GFP; red trace, cplx short-GFP. The NPY-mRFP trace with cplx short-GFP is less noisy because it is an average of more events. (**c**) Averages of outer-circle NPY-mRFP fluorescence traces of the events in **b** normalized to initial-fusion intensity. Black trace, wildtype cplx-GFP; red trace, cplx short-GFP; blue trace, average of 5 events from wildtype cplx-GFP cells showing fastest loss of NPY-mRFP fluorescence, indicating that NPY-mRFP diffusion is unhindered within the space underneath the cell. (**d**) Averaged cplx-GFP signals (from Fig. 1) fitted to single exponential decay from fusion onset. (**e**) Plot of cplx-GFP decay times in **d** and rates of NPY-mRFP release measured with the outer circle fluorescence analysis in **c**. Dashed line, rate of NPY-mRFP release (0.93 ± 0.05 s) with the R59,63E-GFP mutant.
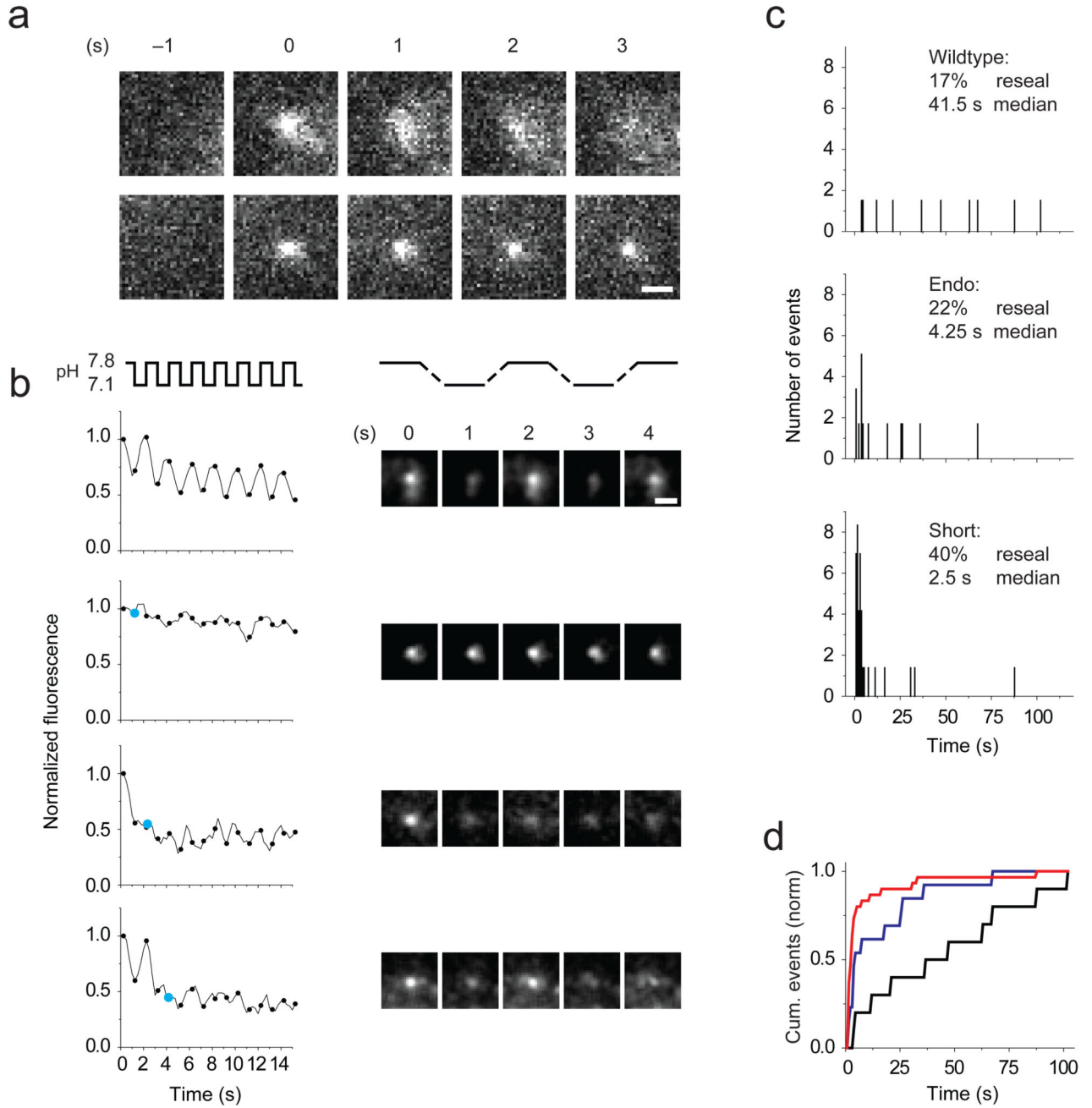
Figure 4.
Rapid resealing of granules with persisting cplx. (**a**) Images (left) of granules labeled with tPA-phluorin spreading (top) or remaining compact (bottom) during exocytosis. Note that phluorin is completely acid-quenched at −1 s before fusion occurs. (**b**) Monitoring granule resealing by alternating the external pH once a second (4 frames). Plots of background-subtracted fluorescence of granules (left) once they become visible through exocytosis. For clarity, only time points marking the end of a pH pulse are shown (black circles), starting 750 ms after fusion. Events were plotted as rolling averages of three frames to reduce noise.

In bottom three events, cyan circles mark the end of the pulse when resealing occurred. Image sequence (right) of the granules analyzed in the left plots. Scale bar, 1 μm. (**c**) Distribution of resealing times with wildtype cplx-mRFP (17% of 60 granules; median time 41.5 s), endogenous cplx (22% of 59; 4.25 s) and cplx short-mRFP (40% of 70; 2.5 s). For each condition, more than 10 cells in 2–4 transfections were analyzed. (**d**) Cumulative frequency distributions of resealing times. Black trace, wildtype cplx-mRFP; red trace, cplx short-mRFP; blue trace, endogenous cplx. *P*<0.001, Kolmogorov-Smirnov tests.
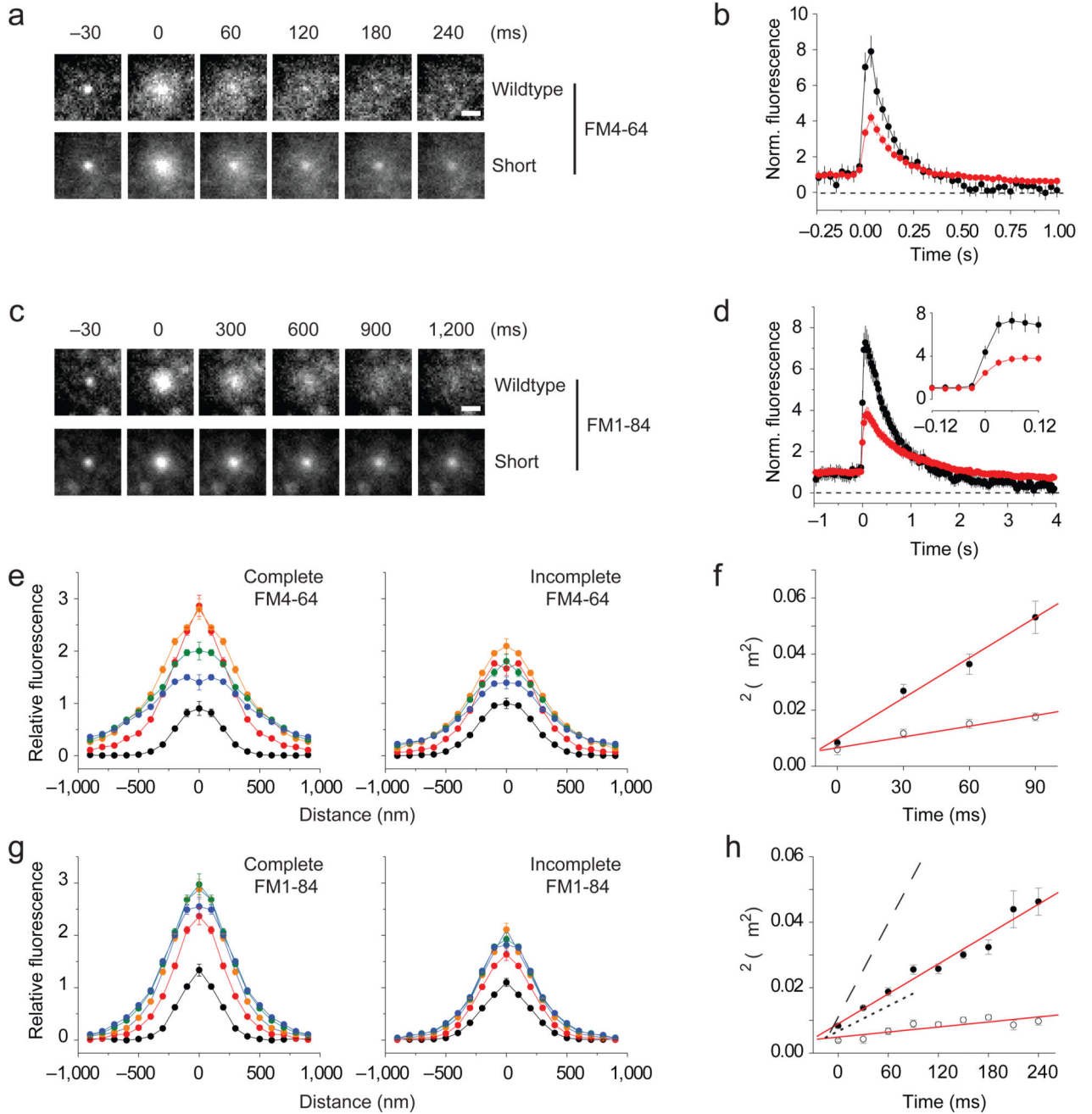
Figure 5.

Restricted lateral diffusion of FM dyes with persisting cplx. (**a**) Averaged image sequence of FM4-64 release with wildtype cplx-GFP (n = 37 events, 7 cells) or cplx short-GFP (n = 78 events, 16 cells). The increase in fluorescence upon fusion is due to changes in the proximity of the dye to the glass interface, as well as changes in the dye's orientation in the membrane. Scale bar, 1 μm. (**b**) Plots of background-subtracted FM4-64 fluorescence of granules, normalized to pre-fusion intensity. Black trace, wildtype cplx-GFP; red trace, cplx short-GFP. (**c,d**) As in **a** and **b**, but with FM1-84 (wildtype cplx-mRFP, n = 34 events, 8 cells;

cplx short-mRFP, *n* = 105 events, 22 cells). Inset, traces shown at an expanded timescale. (**e**) Fluorescence profiles of averaged complete and incomplete FM4-64 release events at selected times relative to fusion (black circles, 30 ms; red circles, 0 ms; orange circles, 30 ms; green circles, 60 ms; blue circles, 90 ms). Images of analyzed events are shown in Supplementary Figure 11.(f). Timecourse of σ^2, the square of the width of Gaussian curves (see Methods). The slope of each line corresponds to an apparent diffusion coefficient (solid circles: complete release, 0.45 μm^2/s; open circles: incomplete release, 0.15 μm^2/s). (**g,h**) As in **e** and **f**, but with FM1-84 (solid circles: complete release, 0.15 μm^2/s; open circles: incomplete release, 0.03 μm^2/s). For comparison, complete and incomplete timecourses of σ^2 with FM4-64 are replotted as dashed and dotted lines, respectively.
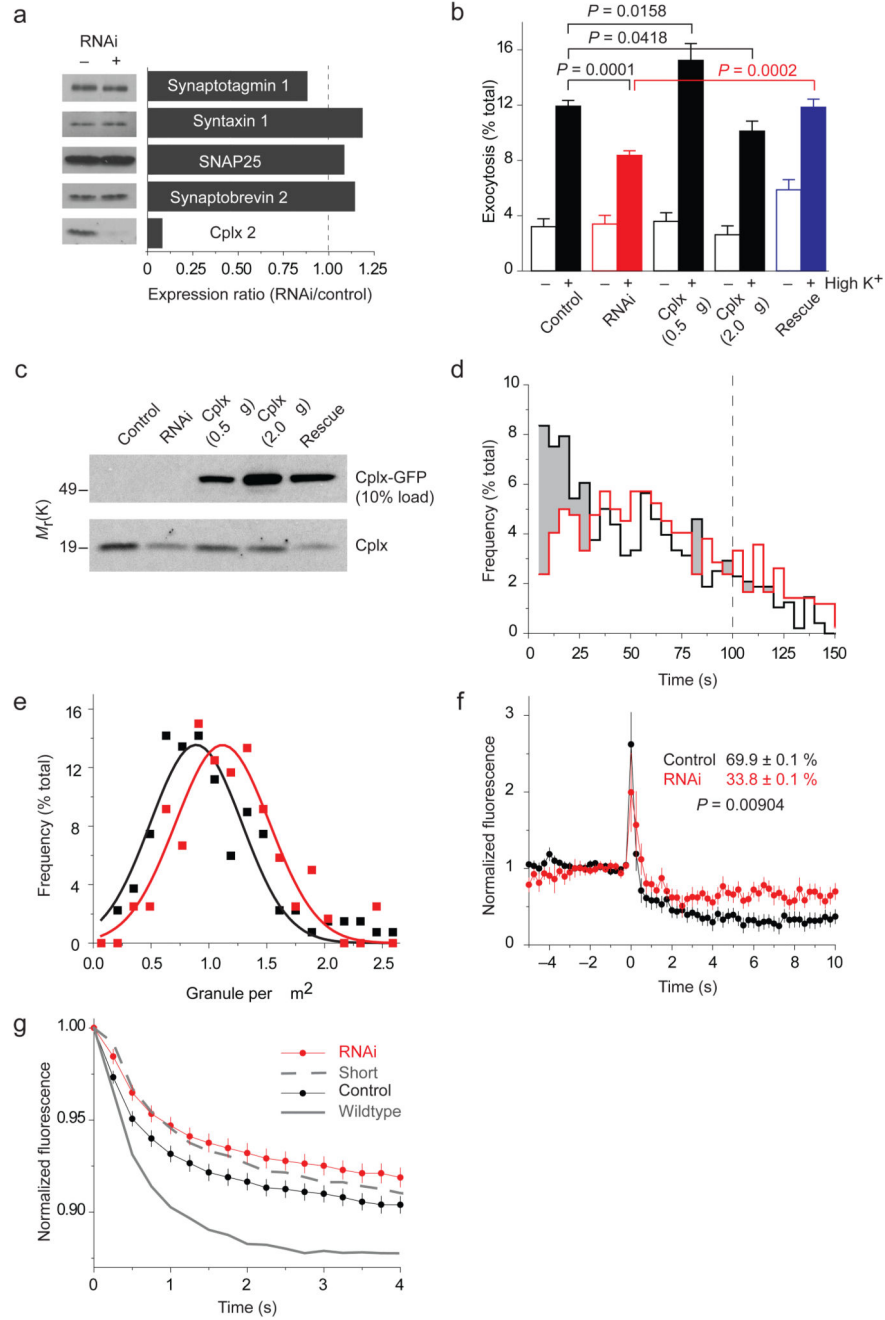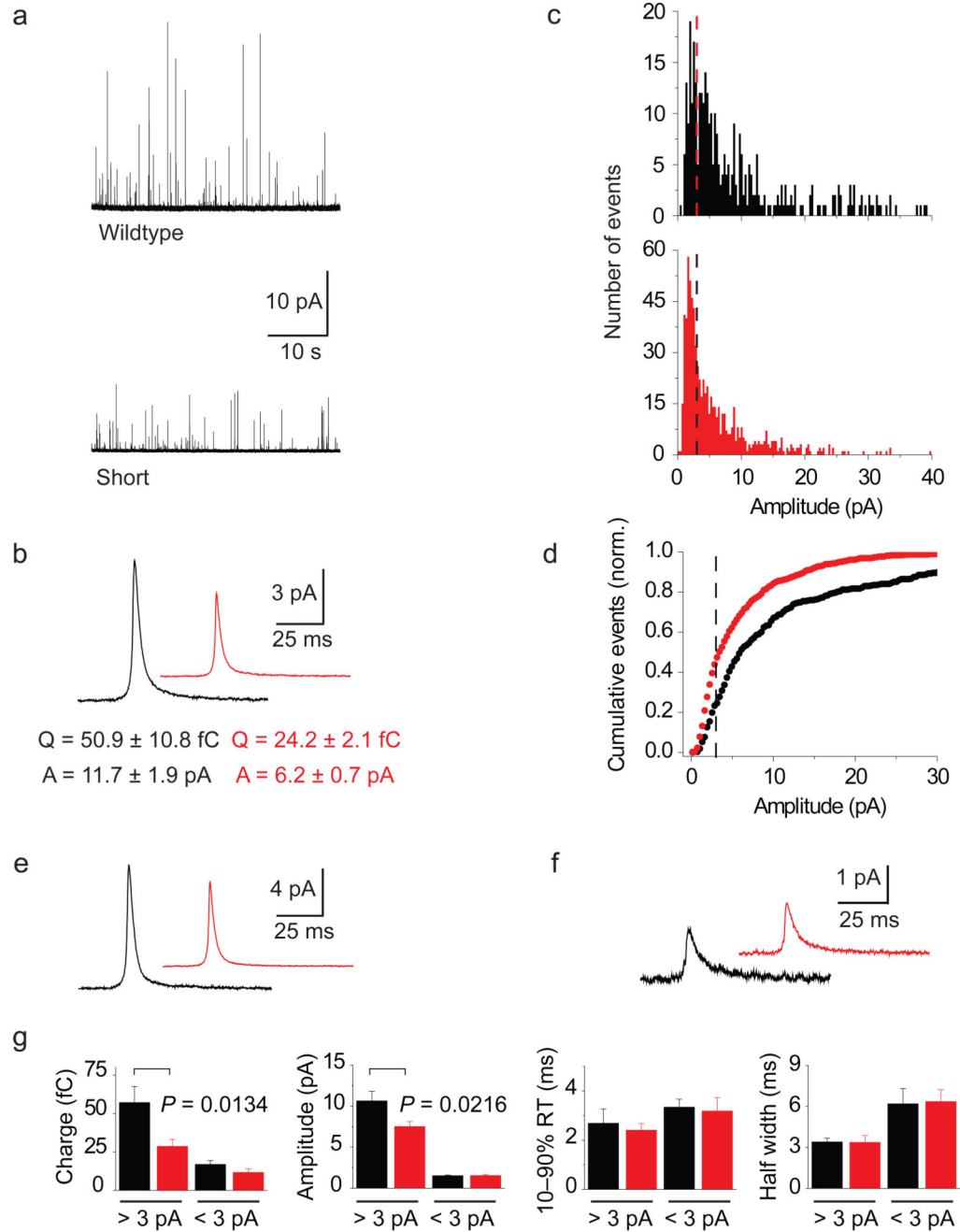
Figure 6.
NPY-mRFP exocytosis in cells depleted of cplx. (**a**) RNAi-mediated silencing of cplx expression. Cells cotransfected with GFP and a plasmid encoding short hairpin RNA (shRNA) targeting cplx 2 were isolated by fluorescence activated cell sorting and analyzed by immunoblotting. (**b**) Fluorimetric assay of NPY-mRFP released by cells after a 45-minute incubation at low or high $[K^+]$ ($n = 15$). In addition to 0.5 μg of NPY-mRFP plasmid (control), cells were transfected with 1 μg shRNA (RNAi), 0.5 or 2.0 μg cplx-GFP, or shRNA and 0.5 μg cplx-GFP plasmids (rescue). (**c**) Immunoblot analysis of the transfection

conditions in **b**. (**d**–**g**) TIRFM imaging of NPY-mRFP exocytosis. (**d**) Fusion latency of stimulus-evoked events in cells with (red, $n = 419$ events) or without shRNA (black, $n = 480$ events). Shading highlights wherever the frequency is lower with shRNA. Time is relative to start of stimulation, which lasted 100 s (dashed line). (**e**) Histogram of granule density in cells with (red) or without shRNA (black). The average density was 1.2 ± 0.5 and 1.0 ± 0.5 granules/μm^2, respectively. (**f**) Background-subtracted fluorescence of granules undergoing exocytosis in cells with or without shRNA. Indicated extents of release (%) were based on cell averages calculated by subtracting the fluorescence 4–5 s after fusion from the intensity during the last 1 s before fusion. (**g**) Outer-circle fluorescence traces of the same events, averaged and normalized to initial-fusion intensity, in cells with or without shRNA. Rates with wildtype cplx-GFP and cplx short-GFP are replotted from Figure 3c.

Figure 7.
Reduced transmitter release with persisting cplx. (**a**) Amperometric recordings of exocytosis from cells expressing wildtype cplx-GFP (upper) or cplx short-GFP (lower). (**b**) Averaged current spikes with wildtype cplx-GFP ($n = 8$ cells) cplx short-GFP ($n = 12$ cells). (**c**) Histograms of spike amplitudes with wildtype cplx-GFP (black) and cplx short-GFP (red). Dashed lines, 3 pA cutoff. (**d**) Distributions in **c**, plotted cumulatively and normalized to the total number of events. Dashed line, 3 pA cutoff. (**e**) Averaged current spikes of events above 3 pA from cells with wildtype cplx-GFP (black) or cplx short-GFP (red). (**f**) Averaged

current spikes of events below 3 pA from cells with wildtype cplx-GFP (black) or cplx short-GFP (red). (**g**) Parameters of events above and below 3 pA with wildtype cplx-GFP (black) and cplx short-GFP (red).